

Experimental demonstration of radicaloid character in a $\text{Ru}^{\text{V}}=\text{O}$ intermediate in catalytic water oxidation

Dooshaye Moonshiram^a, Igor Alperovich^{a,b}, Javier J. Concepcion^c, Thomas J. Meyer^{c,1}, and Yulia Pushkar^{a,1}

^aDepartment of Physics, Purdue University, West Lafayette, IN 47907; ^bResearch Center for Nanoscale Structure of Matter, Southern Federal University, Rostov-on-Don 344090, Russia; and ^cDepartment of Chemistry, University of North Carolina, Chapel Hill, NC 27599

Contributed by Thomas J. Meyer, January 9, 2013 (sent for review June 20, 2012)

Water oxidation is the key half reaction in artificial photosynthesis. An absence of detailed mechanistic insight impedes design of new catalysts that are more reactive and more robust. A proposed paradigm leading to enhanced reactivity is the existence of oxyl radical intermediates capable of rapid water activation, but there is a dearth of experimental validation. Here, we show the radicaloid nature of an intermediate reactive toward formation of the O-O bond by assessing the spin density on the oxyl group by Electron Paramagnetic Resonance (EPR). In the study, an ^{17}O -labeled form of a highly oxidized, short-lived intermediate in the catalytic cycle of the water oxidation catalyst *cis,cis*-[(2,2-bipyridine)₂(H₂O)Ru^{III}ORu^{III}(OH)₂(bpy)₂]⁴⁺ was investigated. It contains Ru centers in oxidation states [4,5], has at least one $\text{Ru}^{\text{V}}=\text{O}$ unit, and shows $|A_{\text{xx}}| = 60\text{G}$ ^{17}O hyperfine splittings (hfs) consistent with the high spin density of a radicaloid. Destabilization of π -bonding in the $d^3 \text{Ru}^{\text{V}}=\text{O}$ fragment is responsible for the high spin density on the oxygen and its high reactivity.

blue dimer | water splitting | catalysis | solar fuels

Water has long been envisioned as a source of protons and electrons for fuel-forming reactions (1, 2), with O₂ the nonpolluting product that is converted back to H₂O in respiration and combustion. The considerable stability of the water molecule, however, hinders realization of artificial photosynthesis in a man-made device. Energetic barriers for water oxidation into O₂ can be lowered by use of a suitable catalyst. The most efficient water oxidation catalyst known to date is Photosystem II, which oxidizes water ($2\text{H}_2\text{O} + 4h\nu \rightarrow \text{O}_2 + 4\text{H}^+ + 4\text{e}^-$) in the process of natural photosynthesis with the help of an Mn₄Ca cluster catalyst embedded in a protein environment (1). Understanding the mechanism of water oxidation is critical for development of alternative energy solutions based on the concept of artificial photosynthesis.

With the aim of uncovering the mechanism of water oxidation, the oxygen evolving complex (OEC) of Photosystem II has been intensively studied by X-Ray Diffraction (XRD) (3–5) and multiple spectroscopic (6–10) and computational approaches (1, 11–15). Intriguingly, Density Functional Theory (DFT) analysis of the reaction barrier for water oxidation in the OEC has shown that formation of the Mn-O• radicaloid intermediate is necessary to reproduce the experimentally observed activation energy (11, 16–19). Several experimental observations are suggestive of the formation of the Mn-O• radicaloid as a species capable of reacting with H₂O with formation of an O-O bond (6, 7), but to the best of our knowledge, no direct experimental demonstration has been reported. The experimental difficulty is in the short lifetime of the S₃ state in the OEC in the Kok cycle for which formation of the Mn-O• radicaloid fragment has been proposed (7, 12, 20), which given its high spin state, makes EPR measurements particularly challenging.

Several Ru-based complexes have been developed as defined molecular catalysts for water oxidation (21–27). The first designed catalyst, the blue dimer (BD) *cis,cis*-(bpy)₂(H₂O)Ru^{III}ORu^{III}(OH)₂(bpy)₂⁴⁺ [bpy is 2,2-bipyridine], shares similarities with the OEC, because they both undergo oxidative activation by proton-coupled electron transfer to reach higher oxidation states where water oxidation occurs (21–24). It is also the most studied catalyst for which experimental data on the reaction mechanism for

water oxidation are available. The results over the past 30 years are summarized in Fig. 1. BD [3,3] and [3,4] are known to be stable forms of the catalyst (numbers in square brackets denote the oxidation state of Ru centers). In BD catalytic cycle, the BD [4,5] and [5,5] intermediates were proposed to be active to O-O bond formation to produce peroxidic intermediates (24, 28–31). DFT analysis of the BD [5,5] intermediate showed unusually high spin density on the oxygen atom of the $d^3 \text{Ru}^{\text{V}}=\text{O}$ fragment (16, 32, 33) and suggested that this property is important for reactivity to water. Here, we show the radicaloid character of the $\text{Ru}^{\text{V}}=\text{O}$ intermediate experimentally by analyzing spin density distribution in the BD [4,5] intermediate. Early reports based on stopped flow measurements pointed to a transient nature of BD [5,5] (34), and we have preliminary data that a species previously reported as BD [5,5] (21, 30) is, indeed, a different form of BD [4,5] (a detailed analysis will be presented elsewhere). EPR results obtained for ^{17}O -labeled BD [4,5] are consistent with the hypothesis of the involvement of a radicaloid intermediate in the activation of water by this Ru-based water oxidation catalyst. Radicaloid character at the oxygen atom in the $\text{Ru}^{\text{V}}=\text{O}$ oxidant, with acceptor orbital largely based on the oxyl group, may facilitate O-O bond formation by extending the electron acceptor wave function to the O atom.

Results and Discussion

The BD catalyst intermediates BD [4,5] and BD [5,5], which are reactive to water, were characterized in previous studies (29, 35–37) and are characterized in more detail in this work. BD [4,5] can be prepared in 0.1 M HNO₃ by oxidation of the BD [3,4] with excess of cerium ammonium nitrate [Ce(IV)] and fast (less than 10–15 s) freezing (37). The BD [4,5] intermediate has been characterized by Ru K-edge X-Ray Absorption Near Edge Structure (XANES) (Fig. 24). Extended X-Ray Absorption Fine Structure (EXAFS) analysis showed a short Ru = O bond (Fig. 2B, Table 1, and Table S1). The protonation state of the Ru^{IV} center in BD [4,5] in 0.1 M HNO₃ (whether it is Ru^{IV}-OH or Ru^{IV}=O) is not known with certainty (24). For example, BD in the [3,4] form, characterized by XRD, contains Ru^{III}-H₂O and Ru^{IV}-OH at pH = 1 (24). EXAFS fits for BD [4,5] were performed to model the protonation states Ru^V=O, Ru^{IV}=O (two short Ru = O distances per BD molecule) versus Ru^V=O, Ru^{IV}-OH (one short Ru = O distance in the BD molecule). A slightly better fit quality was obtained for the Ru^V=O, Ru^{IV}-OH formulation (Table 1, Fig. S1, and Table S1). To further assess the protonation states of BD [4,5], resonance Raman measurements were carried out on frozen BD [4,5] samples prepared by stopped-flow freeze quench of BD [3,4] mixed with 20 eq. of Ce(IV) (Fig. S2). The 816- to 818-cm⁻¹ peak arises from the Ru = O stretch (35, 38, 39) and was observed in samples prepared at 100 ms–7s (Fig. S2), which is in agreement

Author contributions: D.M. and Y.P. designed research; D.M., I.A., and Y.P. performed research; J.J.C. and T.J.M. contributed new reagents/analytic tools; D.M., I.A., and Y.P. analyzed data; and D.M., I.A., T.J.M., and Y.P. wrote the paper.

The authors declare no conflict of interest.

¹To whom correspondence may be addressed. E-mail: tjmeyer@unc.edu or ypushkar@purdue.edu.

This article contains supporting information online at www.pnas.org/lookup/suppl/doi:10.1073/pnas.1222102110/-DCSupplemental.

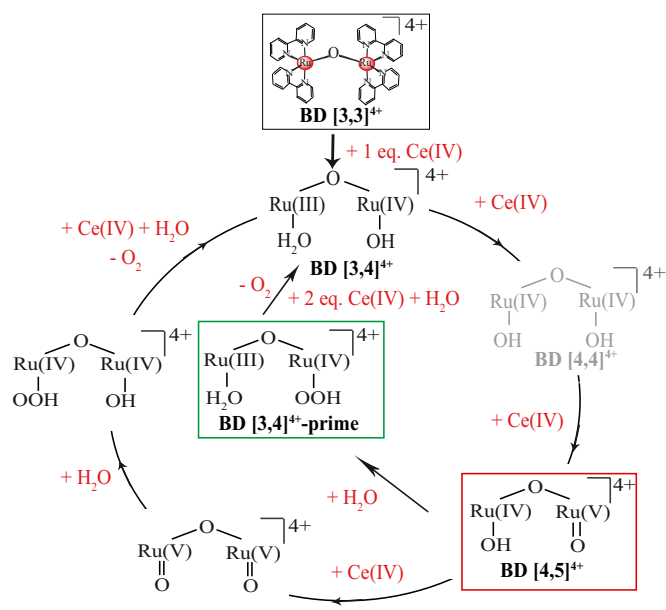


Fig. 1. Catalytic scheme of the water oxidation reactions with BD based on summary of available literature. BD [3,3] and BD [3,4] are stable forms of the catalyst. BD [4,4] has not been characterized and is considered to be unstable. BD [4,5] and BD [5,5] were described as species reactive to water with formation of peroxide species.

with earlier EPR characterization [figure 8 in the work by Moonshiram et al. (37)]. This peak undergoes a 35-cm⁻¹ shift to lower frequency for BD [4,5] prepared in 0.1 M HNO₃/H₂¹⁸O (Fig. S3). Based on earlier literature reports (38, 40), this shift is in good agreement with assignment of the 816-cm⁻¹ band to a Ru^V=O vibration. The 816-cm⁻¹ band grows in relative intensity from 100 ms to 4 s and then decreases after 7 s, giving rise to a band at 683–688 cm⁻¹ previously assigned to a BD [3,4]-prime species (37). At the same time, the band for the Ru-O-Ru bridge mode shifts from 390 (at 4 s) to 410 cm⁻¹ (at 15 s) (37). We were not able to resolve a separate band for the Ru^{IV}=O vibration, likely due to protonation of this group and formation of Ru^{IV}-OH. From these observations, BD [4,5] prepared as described above most likely contains only one Ru=O fragment.

The EPR spectrum of BD [4,5] is shown in Fig. 2C. This signal has been observed earlier (21, 37) and was assigned to a signal from the S = 1/2 spin state with g_{xx} = 2.03, g_{yy} = 1.98, g_{zz} = 1.87 g-tensor; g_{xx} = 2.03 and g_{zz} = 1.87 are clearly resolved in the spectrum, whereas g_{yy} = 1.98 was derived from spectral simulations (Fig. 2C and Fig. S4). Addition of Ru A_{yy} = 40 ± 5G and A_{zz} = 25 ± 5G improves the agreement of simulated and experimental spectra (Fig. S5 A and B). The simulated EPR spectrum in Fig. 2C reflects the isotopic composition for Ru^{99,101} (I = 5/2) (details of EPR simulation in *SI Materials and Methods*). The EPR results are in agreement with earlier experiments for the BD complex prepared in the highly oxidized conditions at pH = 0.5, where apparent Ru^{99,101} hyperfine splitting (hfs) on the order of 40 G were reported (30, 41). A full Ru^{99,101} hfs-tensor was reported for the oxidized Ru^V complex derived from *cis*-[Ru^{II}(bpy)₂(H₂O)₂]²⁺ (42). Notable Ru^{99,101} hfs in BD [4,5] is in agreement with DFT analysis (Table 2), showing considerable spin density on at least one Ru center in BD [4,5].

Samples highly enriched with BD [4,5] can be prepared by the automated freeze quench technique as discussed above (Fig. 2C) (37) or constant potential electrolysis redox titrations with carbon fiber flow electrode (21). However, neither of these approaches can be used for preparation of ¹⁷O-enriched BD [4,5] because of the prohibitive cost of H₂¹⁷O water. ¹⁷O enrichment of BD [3,3] was achieved by dissolution of BD [3,3] powder in 60% enriched H₂¹⁷O and incubation for 24 h. Under such conditions, H₂O molecules

coordinated to Ru centers in BD [3,3] are readily exchangeable (38); 1 eq Ce(IV) in H₂¹⁶O/H₂N¹⁶O₃ solution was added to 1 mM BD [3,3] in 60% enriched H₂¹⁷O to acidify the solution to pH 1 and form BD [3,4]-¹⁷O. Soon after, an excess of Ce(IV) (20 eq.) in H₂¹⁶O/H₂N¹⁶O₃ was added to form BD [4,5]-¹⁷O, and solution was frozen within 30 s. Final H₂¹⁷O enrichment was 50% because of dilutions. ¹⁷O enrichment of the BD molecule is estimated to be between 50% and 60% because of the slower rate of H₂O exchange in BD [3,4]. Thus, we achieved the BD [4,5] intermediate with terminal Ru-O groups labeled with ¹⁷O, whereas bridging oxygen is not exchangeable under conditions of the experiment (21).

The experiment with H₂¹⁷O was repeated two times, and the same EPR spectra were obtained for reaction mixtures. Samples prepared by manual freezing in H₂O (control) and H₂¹⁷O contain up to 50% BD [3,4]-prime species, which are a product of BD [4,5] reaction with water (Fig. 2D). X-Ray Absorption Spectroscopy (XAS) and EPR analysis of this product was reported previously (37). Melting of samples results in complete conversion of BD [4,5] into BD [3,4]-prime intermediate (Fig. 2D). Pure BD [4,5] EPR spectra were extracted by subtracting the contribution of BD [3,4]-prime product from the initial mixture. For BD [4,5] in regular water, spectra obtained by freeze quench and spectra obtained by subtraction were found to be similar (Fig. 2C).

Melting the ¹⁷O samples resulted in the EPR spectrum of BD [3,4]-¹⁷O-prime intermediate (Fig. 3B). Subtraction of the EPR of BD [3,4]-¹⁷O-prime species from the EPR spectrum of the initial mixture allows extraction of the BD [4,5]-¹⁷O spectrum (Fig. 3A). This spectrum is significantly broadened compared with the control, and components of ¹⁷O hfs (I = 5/2) are clearly visible on the low field side of the spectrum (Fig. 3A). Splitting between these components is about 60 G. Upon adding ¹⁷O hfs |A_{xx}| = 60G [taking into account lower estimate (50%) of ¹⁷O enrichment] and using all

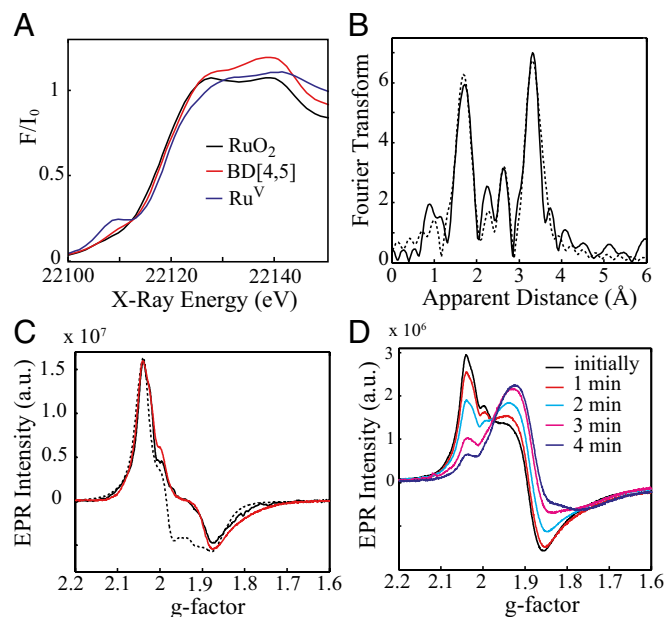


Fig. 2. (A) Normalized Ru K-edge XANES of the BD [4,5] compared with reference compound for Ru^V tetra-*n*-propylammonium bis-2-hydroxy-2ethylbutyrate(oxo) ruthenate(V) and RuO₂. (B) Fourier transforms of k³-weighted Ru EXAFS of the BD [4,5] (black) and EXAFS fit (dashed) with moieties of protonated BD [4,5] [Ru(IV)-OH and Ru(V)=O]. (C) EPR spectra of the BD [4,5] obtained with freeze quench (0.5 mM in 0.1 mol HNO₃, 1-s freezing time; black) and quick manual mixing (1.2 mM in 0.1 mol HNO₃) (Fig. 1) and subtraction of product spectrum (red). Simulation of the BD [4,5] EPR is shown by black dashed line. (D) EPR spectra of the reaction mixture obtained by quick manual mixing of BD [3,4] (1.2 mM in 0.1 mol HNO₃) starting catalyst and 20 eq Ce(IV). BD [4,5] converts into BD [3,4] prime intermediate on sample melting.

Table 1. Structural parameters from EXAFS measurements of the BD [4,5] intermediate

Model species, fit qualities	EXAFS* shell: $N^{**} \times \text{distance}$ (Å)
BD [4,5] in the $\text{Ru}^{\text{V}} = \text{O}$, $\text{Ru}^{\text{IV}} = \text{O}$ protonation state	Ru-N: 4×2.09 Ru-O: 1×1.87
R factor = 0.0003	Ru-O: 1×1.70
Reduced $\chi^2 = 399$	Ru-C: 8×3.02 Ru-O-Ru angle: $166 \pm 2^\circ$ Ru-Ru: 1×3.71
BD [4,5] in the $\text{Ru}^{\text{V}} = \text{O}$, $\text{Ru}^{\text{IV}}\text{-OH}$ protonation state	Ru-N: 4.5×2.09 Ru-O: 1×1.87
R factor = 0.0003	Ru-O: 0.5×1.71
Reduced $\chi^2 = 355$	Ru-C: 8×3.01 Ru-O-Ru angle: $166 \pm 2^\circ$ Ru-Ru: 1×3.71

*For comparison, XRD bond distances are 1.70 Å in Ru^{V} reference compound (49) and 1.81–1.83 Å in complexes with amino ligands (53, 54) with $\text{Ru}^{\text{IV}} = \text{O}$ bond.

** N is the number of vectors given per Ru center.

other parameters as determined by the fit of the EPR spectrum of unlabeled BD [4,5], the experimentally observed splitting A_{xx} could be simulated well (Fig. 3A). There is a rather large uncertainty in the determination of A_{yy} and A_{zz} components of ^{17}O hfs tensor, because they are not clearly resolved. Upper limit for A_{zz} was estimated to be 25 G from analysis of the line broadening of the g_{zz} component. Additional simulations for effect of A_{yy} and A_{zz} values on spectral shape are shown in Fig. S5 C and D. Overall, the EPR data are consistent with the presence of one oxygen center with high spin density. Presence of one oxygen center with high spin density is in agreement with EXAFS and resonance Raman analysis suggesting the $\text{Ru}^{\text{V}} = \text{O}$, $\text{Ru}^{\text{IV}}\text{-OH}$ protonation state for the BD [4,5] intermediate. ^{17}O -pulsed Electron Nuclear Double Resonance (ENDOR) measurements were not possible because of fast relaxation of BD [4,5] species. No echo signals were detected at 10 K for any BD compounds, including BD [3,4]-starting material and [3,4]-prime intermediate.

Earlier theoretical studies of BD [5,5] showed the radicaloid character of the $\text{Ru}^{\text{V}} = \text{O}$ fragment by computing high spin densities on the oxygen (32). We performed DFT analysis of BD [4,5] with three combinations of functional/basis sets (Table 2) to analyze how well DFT can reproduce geometry (Table S2) and magnetic resonance parameters of this molecule. The Ub3lyp/dgdzvp DFT approach predicted an asymmetric structure for the BD molecule with different Ru-O bond distances in the Ru-O-Ru bridge (Table S2), which does not agree with EXAFS results (Table 1). The local density approximation (LDA) with polarized triple- ζ basis set (LDA/TZP) geometry optimization resulted in the structure, which is in a good agreement with EXAFS data (Table S2). Differences in the bond lengths for Ru-O(bridge) and $\text{Ru}^{\text{V}} = \text{O}$ were within 0.05 Å between the experiment and calculation. To further verify how well LDA/TZP can reproduce BD geometry, we calculated the structure of BD [3,4], a molecule with structure that is known from XRD analysis (22, 43). Results are shown in Table S2. DFT simulations done with LDA/TZP closely reproduced geometry of the BD [3,4].

All DFT calculations confirmed the high spin density on the oxygen in the $\text{Ru}^{\text{V}} = \text{O}$ fragment of BD [4,5] (Table 2). Although the sign of experimental $|A_{xx}| = 60\text{G}$ is likely negative, the signs of the A_{yy} and A_{zz} components are not known, preventing us from evaluating the isotropic and anisotropic terms of ^{17}O A-tensor for determination of 2s and 2p spin densities. To overcome this limitation, we computed ^{17}O hfs A-tensor using DFT and compared its values with experiment. Ub3lyp/dgdzvp calculations predicted the ^{17}O hfs A-tensor with two large components: 82.5 G and 66.2 G, which does not agree with experiment. Relativistic LDA/TZP and General-Gradient Approximation XC-functional parametrized by Becke-Ernzerhoff (GGAOPBE)/TZP calculations were carried out with Zeroth-Order Regular Approximation (ZORA). Earlier, these potential/basis sets were used by us to compute electronic structure and Ru L-edge XANES spectra for a model complex $[\text{Ru}(\text{NH}_3)_6]^{3+}$, and BD [3,3], and it was shown that these two basis sets well reproduce experimental XANES (44, 45). LDA/TZP was used here for geometry optimization because of prohibitive computational cost of GGAOPBE/TZP for the BD. Magnetic resonance parameters were evaluated by both LDA and the more sophisticated

Table 2. Spin densities and ^{17}O hfs from DFT analysis

Species	Method, charge, spin	Spin density* on oxygen and Ru	^{17}O hfs from DFT, Gauss	
			a_{iso}	A-tensor
	GW09	O (1) 1.07	O (1) -45.65	$A_{11} = 11.75, A_{22} = -66.18, A_{33} = -82.5$
	unb3lyp	O (2) -0.13		
	/dgdzvp	O (3) -0.16		
	4+, S = 1/2	Ru 1.09		
		Ru -0.86		
	ADF	O (1) 0.68	O (1) -7.95	$A_{11} = -53.17, A_{22} = -0.45, A_{33} = 29.76$
	LDA/TZP	O (2) -0.11		A-tensor in principle axes of g-tensor
	4+, S = 1/2	O (3) 0.01		$A_{xx} = 28.97, A_{yy} = 6.54, A_{zz} = 3.16$
		Ru 0.55		$A_{yx} = 6.54, A_{yy} = -52.30, A_{yz} = -4.02$
		Ru -0.16		$A_{zx} = 3.16, A_{zy} = -4.02, A_{zz} = -0.53$
				g-tensor: $g_{xx} = 2.08, g_{yy} = 2.02, g_{zz} = 1.89$
	OH radical	ADF	O (1) 0.82	O (1) -21.67
GGAOPBE		O (2) -0.21		A-tensor in principle axes of g-tensor
/TZP		O (3) 0.03		$A_{xx} = 12.27, A_{yy} = 2.8, A_{zz} = -17.39$
4+, S = 1/2		Ru 0.57		$A_{yx} = 2.89, A_{yy} = -63.72, A_{yz} = 0.53$
		Ru -0.24		$A_{zx} = -17.39, A_{zy} = 0.53, A_{zz} = -13.57$
				g-tensor: $g_{xx} = 2.11, g_{yy} = 2.02, g_{zz} = 1.90$
OH radical	GW09	O 1.0	-39.17	$A_{11} = 12.10$
	unb3lyp			$A_{22} = 11.16$
	/dgdzvp			$A_{33} = -140.77$
	0, S = 1/2			

*Spin densities were computed using scalar Hamiltonian ZORA approximation, allowing one to perform spin-polarized DFT calculations, whereas EPR properties were extracted from spin-orbit ZORA calculations.

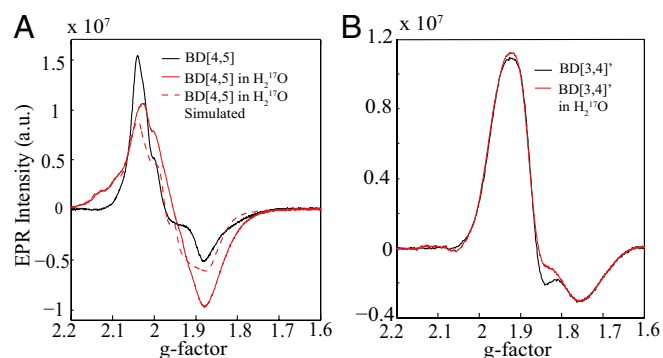


Fig. 3. (A) EPR spectra of BD [4,5] (0.5 mM in 0.1 mol HNO₃) and BD [4,5]-¹⁷O (1.2 mM in 0.1 mol HNO₃) extracted by subtracting EPR spectrum of BD [3,4]-prime and BD [3,4]-¹⁷O-prime (1 mM in 0.1 mol HNO₃) products from initially obtained reaction mixtures. Simulation of the BD [4,5]-¹⁷O spectrum is shown by the red dashed line. (B) Comparison of the EPR spectra of BD [3,4]-prime and BD [3,4]-¹⁷O-prime species (1 mM in 0.1 mol HNO₃).

GGAOPBE approach with no significant difference in results (Table 2). Calculations with both potentials result in somewhat poor agreement for computed and experimental g-tensors, with up to 0.08 deviation for g_{xx} , 0.04 deviation for g_{yy} , and 0.03 deviation for g_{zz} . However, both methods predicted ¹⁷O A-tensor with one large component: -64 G and -53 G (Table 2), which is in good agreement with experiment. The orientation of the g-tensor axis relative to the axis of the BD [4,5] molecule is not known, and will likely remain unknown, as it is not possible to crystallize BD [4,5] due to its short lifetime. Evaluation of the computed ¹⁷O A-tensor in the principle axis of the g-tensor showed that DFT predicts the largest ¹⁷O-hfs along the g_{yy} direction of the g-tensor, which does not agree with experiment. The error likely arises from poor results of the g-tensor calculations. To summarize results of DFT analysis, we can note that (i) all calculations show high spin density on the oxygen in the Ru^V = O fragment; (ii) LAD/TZP and GGAOPBE/TZP reproduce well the largest principle component of the ¹⁷O A-tensor; and (iii) the predictive power of DFT for computation of the g-tensor remains qualitative (46) rather than quantitative, at least for complicated molecules such as the BD with two Ru atoms.

Formation of a π -bond in the M = O fragment was previously discussed in molecular orbital terms (47, 48). We propose that destabilization of π -bonding in the Ru^V = O fragment is responsible for the high spin density on the oxygen. To illustrate this proposed hypothesis, we analyzed MOs with a high contribution of oxygen (from the Ru^V = O fragment) 2p and Ru 4d orbitals, which are responsible for Ru^V = O bonding. MOs analysis of the BD is quite involved because of low symmetry and electronic delocalization. Thus, a simplistic model structure, [RuO(H₂O)₅]³⁺, and an intermediate model, [RuO(OH)(bpy)₂]²⁺, were analyzed, both $S = 1/2$, and parallel to the analysis of BD (Fig. 4, Table 3, and Table S3). In the simplistic model [RuO(H₂O)₅]³⁺, an antibonding orbital (in this case, it is the HOMO) becomes populated with a single electron, and this electron is distributed between oxygen and Ru. Similar orbitals were observed for the intermediate model and BD (Table 3). In all cases, occupied molecular orbitals with significant contribution of the oxygen p-orbitals from the Ru^V = O fragment were identified, which were antibonding for the d^3 Ru^V = O fragment (Table 3). These singly occupied (α) orbitals had their symmetric (β) orbital counter partner among unoccupied orbitals (Table S3), allowing (at least in qualitative terms) an explanation for the high spin density on oxygen. Thus, we are able to understand the origin of the high spin density on the oxygen in the d^3 Ru^V = O fragment. Analysis of the role of the radicaloid oxygen in the activation of H₂O molecule is outside of the scope of this manuscript and will be presented elsewhere.

Although the spectrum of BD [4,5]-¹⁷O is significantly affected by large ¹⁷O splitting, spectra of BD [3,4]-prime and BD [3,4]-¹⁷O-prime intermediates are similar, and no line broadening can be noted. The molecular structure of the BD [3,4]-prime intermediate remains unknown. Previous assignment of the 683-cm⁻¹ band detected in the resonance Raman experiment, which showed a 46-cm⁻¹ shift on ¹⁶O/¹⁸O substitution, to the O-O vibration shifted to an unusual frequency because of coupling with the vibration in the Ru-O-Ru bridge was premature (37). An isotope scrambling experiment in 50% H₂¹⁶O and 50% H₂¹⁸O did not reveal the 1:2:1 intensity pattern expected for the O-O fragment (Fig. S6). This Raman pattern still does not rule out the possibility that the detected vibration is a Ru-O vibration in the Ru-OOH peroxide fragment. Properties of the BD [3,4]-prime intermediate will be analyzed in the future by DFT computation of magnetic resonance parameters and Raman frequencies and by X-ray scattering. Low spin density on oxygen is consistent with a peroxide intermediate with end-on Ru-OOH coordination (Fig. 1). The O-O vibration in such a fragment might have low intensity in the resonance Raman spectrum.

In summary, we have experimentally shown high spin density on the oxygen in the d^3 Ru^V = O fragment of the BD [4,5] intermediate, which is reactive in catalytic water oxidation. We are not aware of other experimental studies of the spin density in M = O units. The Ru^V = O unit is the first to show large radicaloid character and associated large ¹⁷O hfs. Ru^V = O fragment is a radical based on localized ligand orbitals. We cannot exclude that more radicals of this type will be discovered in the future by analysis of highly reactive M = O units with different metal ions with electronic configuration similar to Ru^V = O. DFT calculations reproduce the high spin density on the oxygen in Ru^V = O fragment. The presence of a singly occupied antibonding MO with a high contribution of oxygen p-orbital is responsible for the high spin density on oxygen and its activated radicaloid character. These conclusions suggest that the design of catalysts with partially stabilized oxyl radicals may be an important element in the development of water oxidation catalysts.

Materials and Methods

Sample Preparations. Throughout this study, the BD was used as the PF₆⁻ and ClO₄⁻ salts, and no differences between the two were observed. [(bpy)₂Ru^{III}(H₂O)₂](PF₆)₄ was prepared from [(bpy)₂Ru^{III}(H₂O)₂](ClO₄)₄ as previously described (23). Ultrapure (type 1) water (resistivity 18.2 M Ω ·cm at 25 °C, Total Organic Carbon (TOC) 4 μ g/L) was used for solutions. All samples were prepared in 0.1 M HNO₃ acid pH 1.0 (Catalog number 225711; Sigma Aldrich). The oxidized intermediate BD [4,5] was prepared from BD [3,4] by

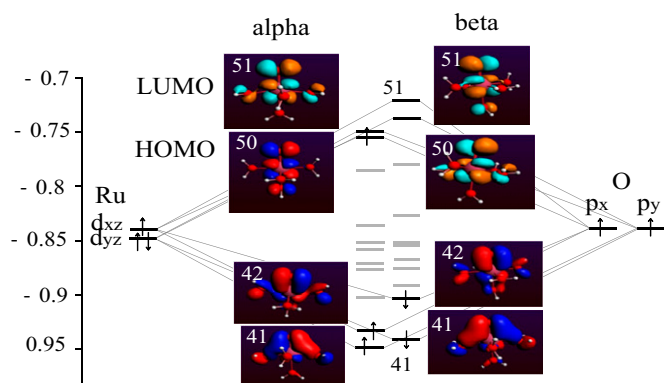
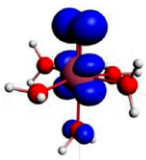
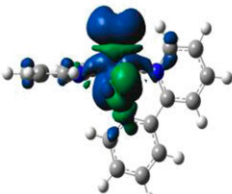

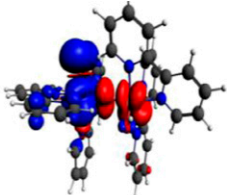
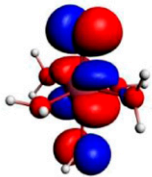
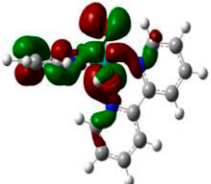
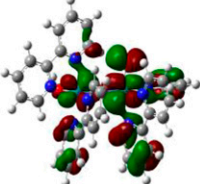
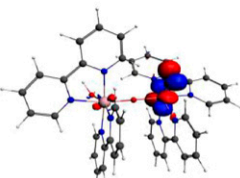


Fig. 4. Schematic MO diagram for [RuO(H₂O)₅]³⁺ model from AFD, LDA/TZP, ZORA, and scalar calculations; more details are in Table S3. Energy of MOs is given in Hartrees (scale on the left); Ru and O atomic orbitals are shown on an arbitrary energy scale. Orbitals essential for Ru^V = O interaction are shown as black levels, and all other levels are gray. Unoccupied orbitals are colored in cyan and orange. An unpaired electron on the HOMO orbital (antibonding for Ru^V = O) is distributed between oxygen and Ru, contributing to considerable spin density on the oxygen in the Ru^V = O fragment.

Table 3. Visualization of spin density and MOs from DFT

Minimal model: RuO(H ₂ O) ₅ ³⁺	Intermediate model: [RuO(OH)(bpy) ₂] ²⁺	BD [4,5]-OH	BD [4,5]-OH*
Spin density on the oxygen in Ru ^V = O fragment			
0.51	0.70	1.06	0.68
Visualization of the spin density			
			
Selected MOs contributing to high spin density on the oxygen.† These MOs have oxygen p character and are antibonding for Ru ^V = O fragment.			
50-α HOMO	110-α HOMO-2	215-α HOMO-4	171-α HOMO
			

Calculations were performed with Gaussian09, unb3lyp/dgdzvp.

*Amsterdam Density Functional (ADF), LDA/TZP, ZORA, scalar ZORA model.

†Molecules were oriented to provide optimal visualization of the MOs localized to Ru^V = O fragment.

oxidation with excess Ce(IV). The reaction mixtures were fast-freeze quenched into a precooled pentane bath (-120 °C) using an SFM 20 Stopped-Flow System (Bio-Logic) equipped with an umbilical connector with a built-in ejection nozzle. For isotopic exchange, BD [3,3] was dissolved in 98% O¹⁸ water and 60% ¹⁷O water (Icon) and incubated for 24 h. The Ru^V = O reference, tetra-n-propylammonium bis-2-hydroxy-2-ethylbutyrate(oxo) ruthenate(V), was prepared as described by Dengel et al. (49). Its EPR spectrum was recorded at 20 K and found to be identical to the spectrum of the original report (49).

EPR Measurements. Low-temperature X-band EPR spectra were recorded using a Bruker EMX X-band spectrometer. The sample temperature was maintained at 20 K, unless otherwise indicated, by use of an Air Products LTR liquid helium cryostat. Spectrometer conditions were as follows: microwave frequency, 9.65 GHz; field modulation amplitude, 10 G at 100 kHz; microwave power, 31.70 mW. Field calibration was checked vs. 2,2,-diphenyl-1-picrylhydrazyl (DPPH) standard. EPR simulations were done with SimFonia software.

XAS and EXAFS Measurements. XAS spectra were collected at the Advanced Photon Source (APS) at Argonne National Laboratory (ANL) on bending magnet beamline 20 at electron energy of 23 keV and average current of 100 mA. The radiation was monochromatized by a Si(110) crystal monochromator. The intensity of the X-rays was monitored by three ion chambers (I₀, I₁, and I₂) filled with 70% nitrogen and 30% argon and placed before (I₀) and after the sample (I₁ and I₂). Plastic (Lexan) EXAFS sample holders (inner dimensions of 12 × 3 × 3 mm) filled with freeze-quenched samples of BD [4,5] were inserted into a precooled (20 K) cryostat. The samples were kept at 20 K in an He atmosphere at ambient pressure. Data were recorded as fluorescence excitation spectra using a 13-element energy-resolving detector. The solid Ru^V sample was diluted with Boron Nitride (BN) powder in a 1:5 ratio, pressed between Mylar tape, and measured in the cryostat in transmission mode. To reduce the risk of sample damage by X-ray radiation, 80% flux was used in the defocused mode (beam size = 1 × 10 mm), and no damage was observed scan after scan to any samples. The samples were also protected from the X-ray beam during spectrometer movements by a shutter synchronized with the scan program. Additionally, low-flux measurements (only 10% of beamline flux) were done on reactive intermediate BD [4,5] to show the same EXAFS results. No more than five scans were taken at each sample position at any condition.

The Ru XAS energy was calibrated by the first maximum in the second derivative of the Ru metal XANES spectrum (22,117 eV). EXAFS scan with 10-eV steps in the

preedge region (21,967–22,102 eV), 1-eV steps (22,102–22,117 eV) through the edge, and 0.05-Å⁻¹ steps from k = 2.0–16 Å⁻¹ were used. As reference compound for BD [4,5], Ru(IV) and Ru(V), Ru(IV) oxide and tetra-n-propylammonium bis-2-hydroxy-2-ethylbutyrate(oxo) ruthenate(V) (49) were used (Fig. 2A). Additional EXAFS analyses are provided in *SI Materials and Methods*.

DFT Calculations. DFT calculations performed with Gaussian09 used B3LYP exchange correlation (XC) functional and dgdzvp basis set, with all electrons of the Ru atom explicitly included in calculations (no frozen cores) (50). For DFT performed with the Amsterdam Density Functional (ADF) 2010 package (51) exploiting Slater-type orbitals expansion as opposed to Gaussian-type ones from Gaussian09 suite, the LDA XC functional parameterized by Vosko et al. (52) and general gradient approximation XC functional parameterized by Becke-Ernzerhoff (GGAOPBE) were used with polarized triple-ζ basis set (LDA/TZP and GGAOPBE/TZP). These basis sets include three Slater functions for each orbital; for Ru atom, it includes two 5p and three more 4f additional polarized functions. No frozen core approximation was used. Relativistic effects were accounted for by simulations within ZORA Hamiltonian. ADF calculations were performed for systems in gaseous phase. All DFT calculation were done for the whole molecules treating all ligands explicitly.

ACKNOWLEDGMENTS. We thank Dr. O. Poluektov and Dr. J. Niklas from ANL, Chemical Sciences and Engineering Division, for help with pulsed EPR measurements and Dr. L. Slipchenko from Purdue University for helpful discussion. We also thank Dr. Y. Chen from the Department of Physics at Purdue University for allowing us to use the Xplora HORIBA Raman Microscope. Access to EPR was provided by Amy Instrumentation Facility, Department of Chemistry, under the supervision of Dr. M. Eversly. Synthesis and characterization (J.J.C.) were supported by the University of North Carolina Energy Frontier Research Center Solar Fuels and Next Generation Photovoltaics, an Energy Frontier Research Center funded by the US Department of Energy, Office of Science, Office of Basic Energy Sciences under Award DE-SC0001011. We thank the US Department of Energy, Office of Basic Energy Sciences for financial support of this work under Grants DE-FG02-06ER15788 (to T.J.M.) and DE-FG02-10ER16184 (to Y.P.) as well as the Ministry of education and science of Russian Federation, Projects 11.519.11.2039, 11.519.11.3005, and 2.5440.2011. Synchrotron facilities were provided by Advanced Photon Source, ANL operated by Department of Energy, Office of Basic Energy Sciences under Contract W-31-109-ENG-38.

1. Wydrzynski T, Satoh S (2005) *Photosystem II: The Light-Driven Water: Plastoquinone Oxidoreductase* (Springer, Berlin).

2. Lewis NS, Nocera DG (2006) Powering the planet: Chemical challenges in solar energy utilization. *Proc Natl Acad Sci USA* 103(43):15729–15735.

3. Ferreira KN, Iverson TM, Maghlaoui K, Barber J, Iwata S (2004) Architecture of the photosynthetic oxygen-evolving center. *Science* 303(5665):1831–1838.
4. Loll B, Kern J, Saenger W, Zouni A, Biesiadka J (2005) Towards complete cofactor arrangement in the 3.0 Å resolution structure of photosystem II. *Nature* 438(7070):1040–1044.
5. Umena Y, Kawakami K, Shen J-R, Kamiya N (2011) Crystal structure of oxygen-evolving photosystem II at a resolution of 1.9 Å. *Nature* 473(7345):55–60.
6. Messinger J, et al. (2001) Absence of Mn-centered oxidation in the S(2) → S(3) transition: Implications for the mechanism of photosynthetic water oxidation. *J Am Chem Soc* 123(32):7804–7820.
7. Pushkar Y, Yano J, Sauer K, Boussac A, Yachandra VK (2008) Structural changes in the Mn₄Ca cluster and the mechanism of photosynthetic water splitting. *Proc Natl Acad Sci USA* 105(6):1879–1884.
8. Yachandra VK, Sauer K, Klein MP (1996) Manganese cluster in photosynthesis: Where plants oxidize water to dioxygen. *Chem Rev* 96(7):2927–2950.
9. Debus RJ, Strickler MA, Walker LM, Hillier W (2005) No evidence from FTIR difference spectroscopy that aspartate-170 of the D1 polypeptide ligates a manganese ion that undergoes oxidation during the S0 to S1, S1 to S2, or S2 to S3 transitions in photosystem II. *Biochemistry* 44(5):1367–1374.
10. Yano J, et al. (2006) Where water is oxidized to dioxygen: Structure of the photosynthetic Mn₄Ca cluster. *Science* 314(5800):821–825.
11. Siegbahn PEM (2008) Theoretical studies of O-O bond formation in photosystem II. *Inorg Chem* 47(6):1779–1786.
12. Siegbahn PEM, Crabtree RH (1999) Manganese oxyl radical intermediates and O-O bond formation in photosynthetic oxygen evolution and a proposed role for the calcium cofactor in photosystem II. *J Am Chem Soc* 121(1):117–127.
13. Messinger J (2004) Evaluation of different mechanistic proposals for water oxidation in photosynthesis on the basis of Mn₄O₄Ca structures for the catalytic site and spectroscopic data. *Phys Chem Chem Phys* 6(20):4764–4771.
14. Pantazis DAO, et al. (2009) Structure of the oxygen-evolving complex of photosystem II: Information on the S(2) state through quantum chemical calculation of its magnetic properties. *Phys Chem Chem Phys* 11(31):6788–6798.
15. Siegbahn PEM (2012) Mechanisms for proton release during water oxidation in the S2 to S3 and S3 to S4 transitions in photosystem II. *Phys Chem Chem Phys* 14(14):4849–4856.
16. Li X, Chen G, Schinzel S, Siegbahn PEM (2011) A comparison between artificial and natural water oxidation. *Dalton Trans* 40(42):11296–11307.
17. Cox N, et al. (2011) Effect of Ca²⁺/Sr²⁺ substitution on the electronic structure of the oxygen-evolving complex of photosystem II: A combined multifrequency EPR, ⁵⁵Mn-ENDOR, and DFT study of the S₂ state. *J Am Chem Soc* 133(10):3635–3648.
18. Siegbahn PEM (2009) Structures and energetics for O₂ formation in photosystem II. *Acc Chem Res* 42(12):1871–1880.
19. Siegbahn PEM (2008) A structure-consistent mechanism for dioxygen formation in photosystem II. *Chemistry* 14(27):8290–8302.
20. Boussac A, Sugiura M, Rutherford AV, Dorlet P (2009) Complete EPR spectrum of the S₃-state of the oxygen-evolving photosystem II. *J Am Chem Soc* 131(14):5050–5051.
21. Cape JL, Lymar SV, Lightbody T, Hurst JK (2009) Characterization of intermediary redox states of the water oxidation catalyst, [Ru(bpy)₂(OH)₂]₂O⁴⁺. *Inorg Chem* 48(10):4400–4410.
22. Gilbert JA, et al. (1985) Structure and redox properties of the water-oxidation catalyst [(Bpy)₂(OH)₂RuORu(OH)₂(Bpy)]⁴⁺. *J Am Chem Soc* 107(13):3855–3864.
23. Gersten SW, Samuels GJ, Meyer TJ (1982) Catalytic oxidation of water by an oxo-bridged ruthenium dimer. *J Am Chem Soc* 104(14):4029–4030.
24. Liu F, et al. (2008) Mechanisms of water oxidation from the blue dimer to photosystem II. *Inorg Chem* 47(6):1727–1752.
25. Romero I, et al. (2008) Ru complexes that can catalytically oxidize water to molecular dioxygen. *Inorg Chem* 47(6):1824–1834.
26. Zong R, Thummel RP (2005) A new family of Ru complexes for water oxidation. *J Am Chem Soc* 127(37):12802–12803.
27. Duan L, et al. (2012) A molecular ruthenium catalyst with water-oxidation activity comparable to that of photosystem II. *Nat Chem* 4(5):418–423.
28. Lei YB, Hurst JK (1994) Structural investigations of the catalytic mechanisms of water oxidation by the [(bpy)₂Ru(OH)₂]₂O⁴⁺ ion. *Inorg Chem* 33(20):4460–4467.
29. Hurst JK, Zhou J, Lei Y (1992) Pathways for water oxidation catalyzed by the [(bpy)₂Ru(OH)₂]₂O⁴⁺ ion. *Inorg Chem* 31(6):1010–1017.
30. Hurst JK, Cape JL, Clark AE, Das S, Qin CY (2008) Mechanisms of water oxidation catalyzed by ruthenium diimine complexes. *Inorg Chem* 47(6):1753–1764.
31. Concepcion JJ, Jurss JW, Templeton JL, Meyer TJ (2008) Mediator-assisted water oxidation by the ruthenium “blue dimer” cis,cis-[(bpy)₂(H₂O)RuORu(OH)₂(bpy)₂]⁴⁺. *Proc Natl Acad Sci USA* 105(46):17632–17635.
32. Yang X, Baik MH (2006) cis,cis-[(bpy)₂RuVO]₂O⁴⁺ catalyzes water oxidation formally via in situ generation of radicaloid RuIV-O. *J Am Chem Soc* 128(23):7476–7485.
33. Bianco R, Hay PJ, Hynes JT (2011) Theoretical study of O—O single bond formation in the oxidation of water by the ruthenium blue dimer. *J Phys Chem A* 115(27):8003–8016.
34. Chronister CW, Binstead RA, Ni J, Meyer TJ (1997) Mechanism of water oxidation catalyzed by the μ-oxo dimer [(bpy)₂(OH)₂Ru^{III}ORu^{III}(OH)₂(bpy)₂]⁴⁺. *Inorg Chem* 36(18):3814–3815.
35. Yamada H, Hurst JK (2000) Resonance Raman, optical spectroscopic, and EPR characterization of the higher oxidation states of the water oxidation catalyst, cis,cis-[(bpy)₂Ru(OH)₂]₂O⁴⁺. *J Am Chem Soc* 122(22):5303–5311.
36. Binstead RA, Chronister CW, Ni JF, Hartshorn CM, Meyer TJ (2000) Mechanism of water oxidation by the μ-oxo dimer [(bpy)₂(H₂O)(Ru^{III}ORu^{III}(OH)₂(bpy)₂]⁴⁺. *J Am Chem Soc* 122(35):8464–8473.
37. Moonshiram D, et al. (2012) Structure and electronic configurations of the intermediates of water oxidation in blue ruthenium dimer catalysis. *J Am Chem Soc* 134(10):4625–4636.
38. Yamada H, Koike T, Hurst JK (2001) Water exchange rates in the diruthenium μ-oxo ion cis,cis-[(bpy)₂Ru(OH)₂]₂O⁴⁺. *J Am Chem Soc* 123(51):12775–12780.
39. Yamada H, Siems WF, Koike T, Hurst JK (2004) Mechanisms of water oxidation catalyzed by the cis,cis-[(bpy)₂Ru(OH)₂]₂O⁴⁺ ion. *J Am Chem Soc* 126(31):9786–9795.
40. Rhee IR, Nakamoto K (1990) Resonance Raman spectra of reaction intermediates in the oxidation process of ruthenium(II) and iron(II) porphyrins. *J Am Chem Soc* 112(9):3289–3297.
41. Cape JL, Hurst JK (2008) Detection and mechanistic relevance of transient ligand radicals formed during [Ru(bpy)₂(OH)₂]₂O⁴⁺-catalyzed water oxidation. *J Am Chem Soc* 130(3):827–829.
42. Planas N, et al. (2011) Electronic structure of oxidized complexes derived from cis-[Ru(II)(bpy)₂(H₂O)₂]²⁺ and its photoisomerization mechanism. *Inorg Chem* 50(21):11134–11142.
43. Schoonover JR, Ni JF, Roecker L, Whiter PS, Meyer TJ (1996) Structural and resonance Raman studies of an oxygen-evolving catalyst. Crystal structure of [(bpy)₂(H₂O)Ru^{III}ORu^{III}(OH)(bpy)₂](ClO₄)⁴⁻. *Inorg Chem* 35(20):5885–5892.
44. Alperovich I, et al. (2011) Understanding the electronic structure of 4d metal complexes: From molecular spinors to L-edge spectra of a di-Ru catalyst. *J Am Chem Soc* 133(39):15786–15794.
45. Alperovich I, Soldatov A, Moonshiram D, Pushkar Y (2012) Density functional theory simulation of the L_{2,3} XANES spectra. *JETP Lett* 95(10):504–510.
46. Saladino AC, Larsen SC (2005) DFT calculations of EPR parameters of transition metal complexes: Implications for catalysis. *Catal Today* 105(1):122–133.
47. Ballhausen CJ, Gray BH (1961) The electronic structure of the vanadyl ion. *Inorg Chem* 1(1):111–122.
48. Betley TA, Wu Q, Van Voorhis T, Nocera DG (2008) Electronic design criteria for O-O bond formation via metal-oxo complexes. *Inorg Chem* 47(6):1849–1861.
49. Dengel AC, Griffith WP, Omahoney CA, Williams DJ (1989) A stable ruthenium(V) oxo complex—x-ray crystal-structure and oxidizing properties of tetra-n-propylammonium bis-2-hydroxy-2-ethylbutyrate(Oxo)-ruthenate(V). *J Chem Soc Chem Commun* 1(22):1720–1721.
50. Godbout N, Salahub DR, Andzelm J, Wimmer E (1992) Optimization of Gaussian-type basis sets for local spin density functional calculations. Part I. Boron through neon, optimization technique and validation. *Can J Chem* 70(2):560–571.
51. Velde GT, et al. (2001) Chemistry with ADF. *J Comput Chem* 22(9):931–967.
52. Vosko SH, Wilk L, Nusair M (1980) Accurate spin-dependent electron liquid correlation energies for local spin-density calculations—A critical analysis. *Can J Phys* 58(8):1200–1211.
53. Cheng W-C, Yu W-Y, Cheung K-K, Che C-M (1994) Syntheses of novel monomeric 1,4,7-trimethyl-1,4,7-triazacyclononane ruthenium complexes. Reactivities and structure of sterically encumbered cationic monoquaruthenium(II) and monooxoruthenium(IV) complexes. *J Chem Soc Dalton Trans* 23(1):57–62.
54. Welch TW, Ciftan SA, White PS, Thorp HH (1997) Electron-rich oxoruthenium(IV) cleavage agents: A zero-order rate law for DNA catalysis. *Inorg Chem* 36(21):4812–4821.